Available online at www.sciencedirect.com
SCIENCE DIRECT®
Wear 256 (2004) 735–746
WEAR
www.elsevier.com/locate/wear

Mechanisms governing the high temperature erosion of thermal barrier coatings

X. Chen [a,*], M.Y. He [b], I. Spitsberg [c], N.A. Fleck [d], J.W. Hutchinson [e], A.G. Evans [b]

[a] *Department of Civil Engineering and Engineering Mechanics, Columbia University, New York, NY 10027, USA*
[b] *Materials Department, University of California, Santa Barbara, CA 93106, USA*
[c] *GE Aircraft Engines, Cincinnati, OH 45215, USA*
[d] *Department of Engineering, University of Cambridge, Cambridge, CB2 1PZ, UK*
[e] *Division of Engineering and Applied Sciences, Harvard University, Cambridge, MA 02138, USA*

Received 17 March 2003; accepted 6 June 2003

Abstract

The impact of thermal barrier coatings by hard projectiles at high temperature has been analyzed. Three different domains have been explored: each differentiated by particle size, velocity, temperature and TBC composition. *Domain I* applies when the projectile creates deeply penetrating plastic/densification zones. In this case, short time elastic effects are relatively unimportant. The response is dominated by stresses that arise after about 1 ms, at particle rebound. Deformation incompatibilities nucleate delaminations: which thereafter, extend in the TBC just above the interface with the TGO. An index governing material removal by delamination has been derived as $\Xi_1 = \Gamma_{\rm TBC} E_{\rm TBC}^2/(\sigma_Y^{\rm TBC})^3$, where $\Gamma_{\rm TBC}$ is the toughness of the TBC, $E_{\rm TBC}$ its Young's modulus and $\sigma_Y^{\rm TBC}$ its yield strength. In *Domain II* the plastic wave intensity is below the delamination threshold: whereupon a thin densified zone is formed, without severe cracking. Subsequent impacts induce elastic bending of the neighboring columns. The bending develops at short times (10–50 ns), causing large, transient stresses at the intersection between the dense and underlying columnar layers. These stresses can be large enough to form cracks that remove the dense layer. Analysis of this effect identifies an erosion index: $\Xi_2 \equiv \Gamma_{\rm TBC}/E_{\rm TBC}^{3/5}\, d\sigma_Y^{\rm TBC}$, where d is the column diameter. Large values of Ξ_2 reduce the erosion rate. *Domain III* arises for impact conditions that elicit an entirely elastic response in the TBC. The domain applies at low temperature and when the impacting particles are small. Again, bending effects at the tops of the columns arise at short times. Another erosion index arises, $\Xi_3 \equiv \Gamma_{\rm TBC}/E_{\rm TBC}^{3/5}\, d$, differing from that in Domain II because plasticity is not involved.

Keywords: Thermal barrier coating; Impact; Erosion; Cracking; Delamination; Stress wave

1. Introduction

Thermal barrier systems used in gas turbines consist of a tri-layer [1–5]. The outer layer is typically yttria-stabilized zirconia (YSZ). A thermally grown oxide (TGO) exists between the YSZ and a Ni(Al) alloy sub-layer, known as a bond coat [1–5]. Such systems exhibit multiple failure modes [5–9]. Prior assessments have focused primarily on modes governed by the energy density in the thermally grown oxide, which causes failure by either large-scale buckling or edge delamination [5–10]. Among other modes, foreign object damage (FOD) [11] is particularly important, as well as gradual erosion of the surface [12–14]. The focus of this article is on the mechanisms governing FOD and erosion at surface temperatures that pertain during turbine operation (about 1200 °C). At these temperatures, the YSZ is susceptible to plastic deformation [11].

The approach used to unearth the mechanisms is as follows. Dynamic simulations are performed of a high velocity object penetrating the TBC. The displacements, the extent of the plastic deformation and the induced stresses are all determined. Thereafter, the stresses are related to cracking phenomena by using fracture mechanics concepts. The emphasis is on materials made by electron beam physical vapor deposition (EB-PVD), which exhibit a columnar microstructure (Figs. 1 and 2). This microstructure is included in the simulations.

Erosion and wear processes are notoriously difficult to model, quantitatively. Accordingly, the present paper has the more limited objectives of: (a) identifying domains in which three different mechanisms govern erosion and (b) gaining enough understanding to ascertain microstructure and property changes that might affect erosion rates within

* Corresponding author. Tel.: +1-212-854-3787; fax: +1-617-496-0601.
E-mail address: xichen@civil.columbia.edu (X. Chen).

0043-1648/$ – see front matter © 2003 Elsevier B.V. All rights reserved.
doi:10.1016/S0043-1648(03)00446-0

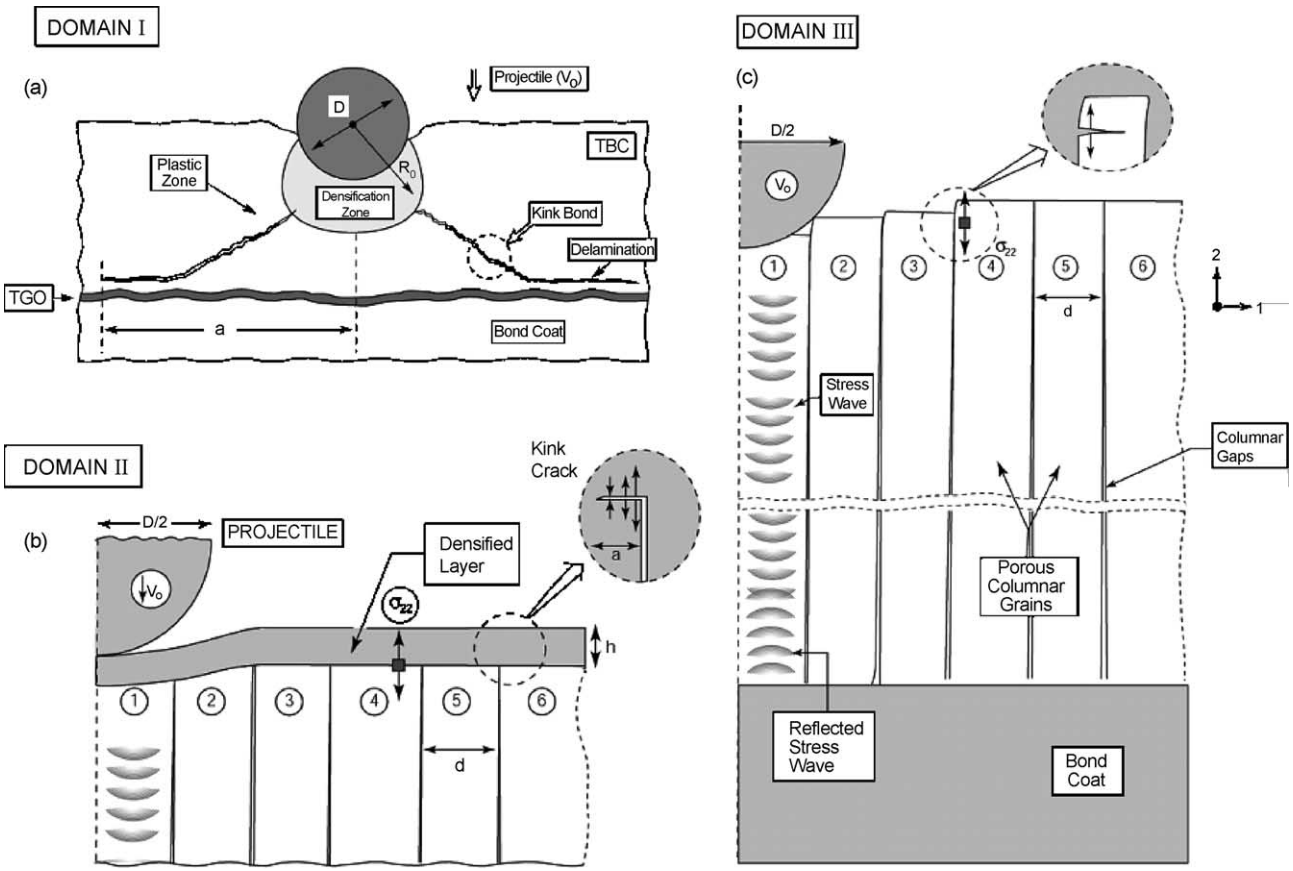

Fig. 1. Schematics showing the responses that occur within the three erosion Domains: (a) delamination occurring in response to an impact that induces a deeply penetrating plastic zone; (b) the elastic response that arises in Domain II when a thin dense layer is created by prior multi-particle impacts; (c) the elastic response in Domain III showing the bending of the tops of the columns to accommodate the particle penetration.

each domain. Explicit connections between material properties and erosion will be addressed in a separate article [15].

2. A synopsis of observations and mechanisms

Observations of cross-sections through EB-PVD materials eroded at high temperature (typically 1150 °C) have suggested multiple mechanisms of material removal, dictated by particle size, velocity, temperature and material [11–14]. The mechanisms are distinguished by time scales for stress wave transit relative to those for plastic deformation (Fig. 1). The details will emerge as the simulations unfold in the following sections.

Domain I. When large particles impact with high momentum at high temperature, most of the kinetic energy is absorbed by plastic deformation and densification of the TBC (Fig. 1a) [11]. The deformation may be accompanied by kink bands around the perimeter of the plastic zone [11]. When present, these bands intersect the TGO, and initiate delamination cracks that extend outward from the impact center, parallel to the interface (Figs. 1c and 2c). In this domain, the stresses and deformations are dominated by the plasticity, which reaches its fullest extent at maximum penetration, just before rebound (time scales of order 1 ms) [11]. Rate effects are secondary. The important phenomena can be ascertained from quasi-static analogs in monolithic ceramics [16–18].

Domain II. At intermediate particle size and lower momentum, the dense zone is too shallow to nucleate a delamination. Instead, successive impacts form a densified thin layer (Figs. 1b and 2a and b). Subsequent impacts induce stress concentrations at the intersection of the dense and columnar regions, which cause portions of the dense layer to detach from the underlying columns. The stresses affecting such cracking are induced at short times (of order 10 ns) and governed by elastic waves. Later in the penetration, plasticity and densification reinstate the dense layer (again, time scales of order 1 ms).

Domain III. At either low particle size/momentum or lower temperature, a continuous dense layer does not form and the columns remain separate. The response is elastic and zones of local tensile stress develop near the surface in columns adjacent to the impact site, caused by column bending as the projectile penetrates (Fig. 1c). These stresses cause the tops of the columns to detach. The time scales are again short enough (∼10 ns) that the stresses causing material are dominated by elastic waves.

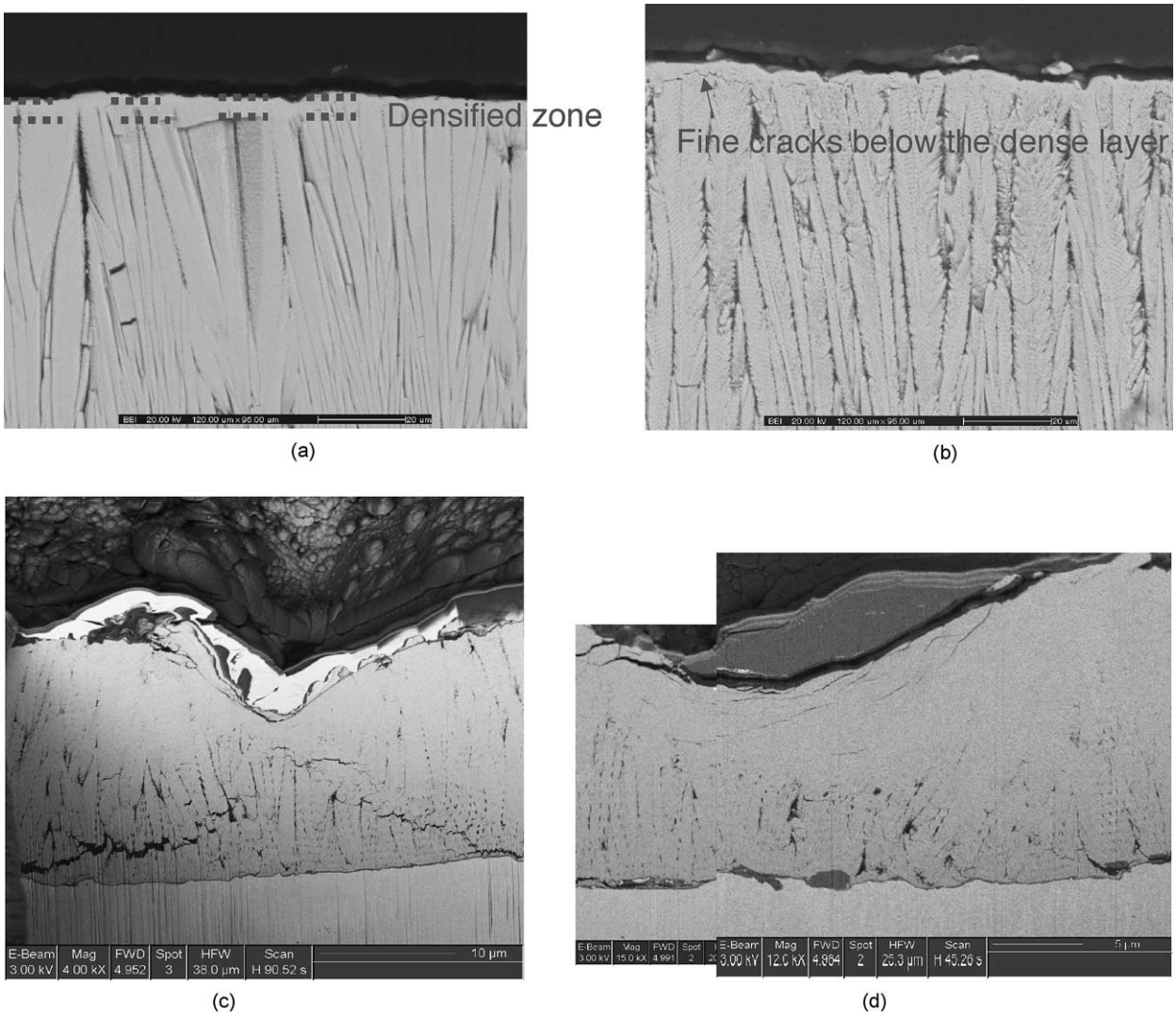

Fig. 2. Scanning electron images of cross-sections of specimens that reveal responses in Domains I and II [11]. (a) The densified layer that forms in Domain II. (b) Small inter-columnar cracks sometimes observed beneath the dense layer in Domain II. (c) The relatively large densified zone and kink band that form in Domain I. A delamination nucleates where the kink band intersects the TGO [11]. (d) An example of an intermediate Domain I/II response showing a dense zone, absent kink bands and delaminations, containing a distribution of circumferential cracks. Note that a section of the impacting particle remains attached to the crater [11].

Domain I/II. There may be a mechanism intermediate between Domains I and II (Fig. 2d) [11]. Namely, within the densified zone created during impact, if some of the particle remains attached during rebound, radial tensile stresses develop that induce a series of circumferential cracks within the dense zone. These cracks coalesce to cause material removal.

Developing a full simulation capability for erosion is notoriously difficult, even for homogeneous solids. The difficulty arises because of the interactions that occur between deformations and cracking events caused by multiple impacts. Where possible, the approach is to establish a ‘steady-state’ condition induced in the material following multi-particle impact and then ascertain the consequences of a small number of subsequent impacts, including the further deformation, the formation of cracks and the occurrence of material removal. In Domain II, this “state” includes a dense upper layer (Figs. 1b and 2a and b). In domains I and III, the columns are in a pristine state prior to impact.

3. Some related experimental observations

Burner rig specimens that have experienced material removal by high temperature erosion have been cross-sectioned and examined by scanning electron microscopy [11,19]. Typical observations are summarized in Fig. 2. A central finding is that a layer of dense material often exists beneath the eroded surface [11]. This happens because the porosity is removed by “dynamic hot pressing”, caused by the hydrostatic compression induced beneath the impacting particles, combined with the capacity of YSZ to

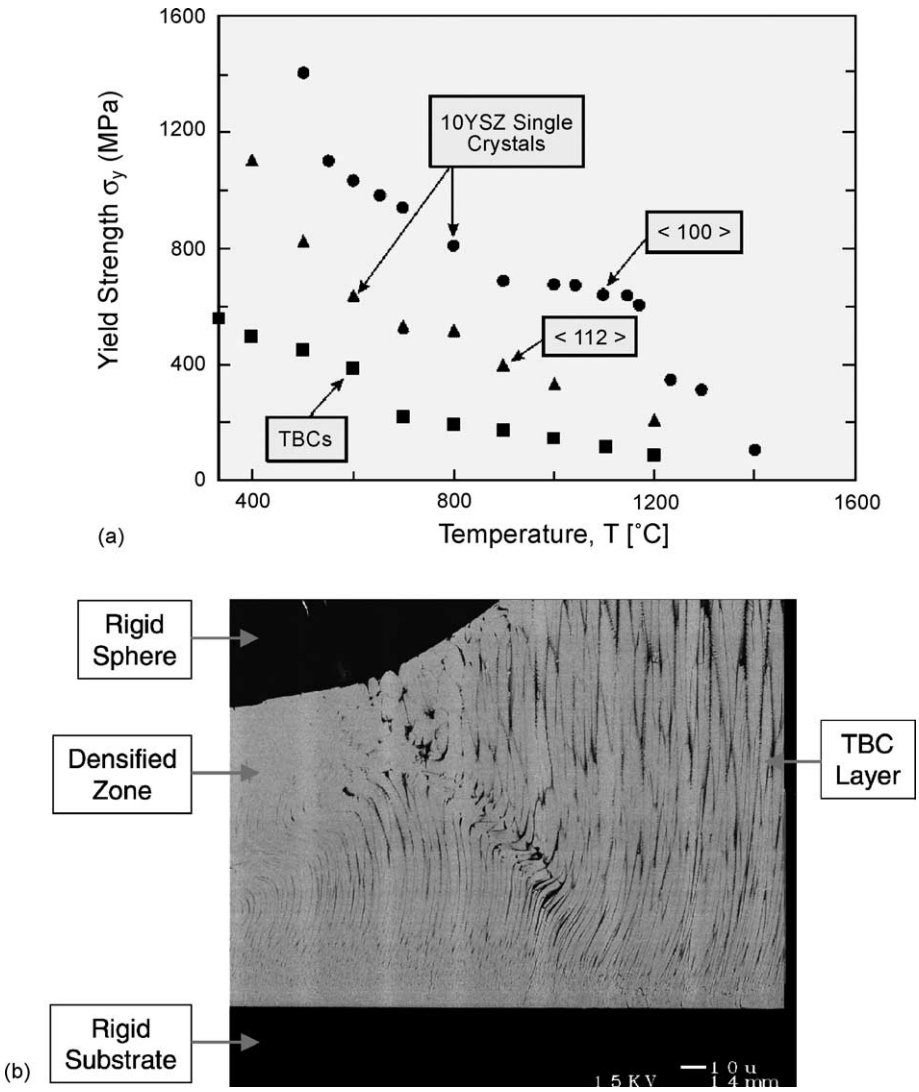

Fig. 3. (a) The yield strength of yttria-stabilized zirconia as a function of temperature [20,21]. (b) A cross-section of a columnar 7YSZ after testing 1150 °C [20], showing the densification and the kink bands, as well as the plastic deformation of the columns.

exhibit plastic deformation. The depth of the dense layer is determined by the high temperature yield strength of the YSZ (Fig. 3a) [20,21]. Cross-sections (Fig. 3b) vividly illustrate the densification and plastic deformation that accompany penetration, as well as the development of kink bands.

In Domain I, characterized by observable impressions on the surface, the dense zone is large, $h_D > 10\,\mu m$ [11], and is accompanied by associated kink bands and delamination (Fig. 2c). In Domain II, the dense layer thickness is in the range, $1\,\mu m \leq h_D \leq 5\,\mu m$ (Fig. 2a). Some cross-sections indicate that microcracks form at the transition between the dense layer and the underlying columnar microstructure [14] (Fig. 2b). It is surmised that the coalescence of these microcracks upon subsequent impacts detaches the dense layer and causes material removal. The intermediate Domain I/II with radial cracks present in the dense zone is demonstrated in Fig. 2d. Note that some of the projectile is still attached.

4. The model

The model is axisymmetric, as depicted in Fig. 1b and c. The columnar microstructure is incorporated as a series of concentric layers with a physical gap between each. The role of contact between neighboring columns during impact is explored by regarding these regions as either frictionless or subject to a friction coefficient of unity. The material within the columns incorporates porosity at the 20% level. The thickness of the TBC ($H = 100\,\mu m$) and the column width ($d = 5\,\mu m$) are both fixed for most calculations. A few results are obtained with wider columns ($d = 10\,\mu m$). The columns are imparted isotropic physical properties (Young's modulus, $E_{TBC} = 140\,GPa$; Poisson's ratio, $\nu_{TBC} = 0.2$). At the operating condition, the bond coat is susceptible to plastic deformation [20,21], with high temperature (1150 °C) yield strength at low strain rates, $\sigma_Y^{TBC}(0) = 100\,MPa$.

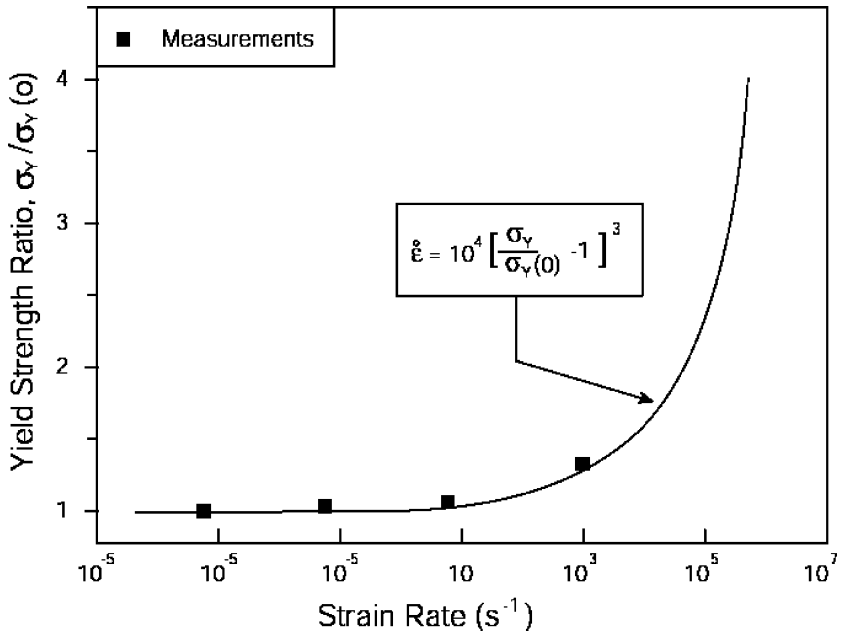

Fig. 4. The strain-rate dependence of the yield strength for typical alloys [22]. The behavior used for YSZ is superposed.

Previous assessments [22] have indicated that the strain-rate sensitivity of the plastic deformation can be an especially important aspect of the response. The rate-dependent responses of the YSZ and of the bond coat are not known. Absent actual data, it is assumed to be similar to that for metals, such as Ti alloys (Fig. 4). The flow stress at low rates, beneath the "knee", designated $\sigma_Y^{\mathrm{TBC}}(0)$, is calibrated using the high temperature stress/strain data for YSZ (Fig. 3). That for the bond coat, σ_Y^{TBC}, is determined from tensile test data [21]. The change to high rate sensitivity is considered to occur at a strain-rate, $\dot{\varepsilon} = 10^4/\mathrm{s}$, with rate exponent at higher rates, $n = 3$ (Fig. 4).

The rotation of the turbine results in impact velocities, $v_0 \approx 300\,\mathrm{m/s}$. The particle size and properties vary over a range. For the present assessment, the particle diameter is in the range, $D = 20$–$50\,\mu\mathrm{m}$. The dominant particles are assumed to have density, $\rho_\mathrm{p} = 4000\,\mathrm{kg/m^3}$, representative of the alumina used in the erosion tests [14]. In the turbine itself, the particles would have different density.

Based on these material parameters and geometric configurations, the stresses and displacements in the TBC caused by impact are calculated using the commercial finite element code ABAQUS explicit [23]. Since the calculations are confined to a specific velocity and particle density, trends that arise upon major changes in impact conditions cannot be inferred. The scaling parameters identified below are intended to highlight the influence of the TBC properties, within a range of impact conditions relevant to turbine operation.

5. Non-dimensional parameters

(i) *Substrates subject to plastic deformation*. Simulations of particle impacts that induce plastic deformations have identified several key non-dimensional groups and relationships between them. The impact energy can be normalized as [11,24]:

$$\Omega = \left(\frac{\pi}{12}\right)\left[\frac{\rho_\mathrm{p}}{\sigma_Y^{\mathrm{TBC}}(0)}\right] v_0^2 \tag{1}$$

The maximum penetration of the projectile, $\delta_{\max}$, into a rate-independent, dense substrate is related to Ω by [24]:

$$\frac{\delta_{\max}}{D} = 0.33\sqrt{\Omega}(0.1 + 0.24\sqrt{\Omega}) \tag{2}$$

Porosity in the material increases the penetration. The influence has been assessed for a rate-independent material having initial porosity, $f_0 = 0.2$. The result is [11]:

$$\frac{\delta_{\max}}{D} = 0.38\sqrt{\Omega}(0.1 + 0.84\sqrt{\Omega}) \tag{3}$$

The corresponding result for a rate-dependent porous material has yet to be assessed because of limitations of the available numerical software.

The depth, h_D, of the densified zone scales with the penetration as [11]:

$$h_\mathrm{D} \approx 4\sqrt{\delta_{\max} D} \tag{4}$$

(ii) *Substrates subject to elastic deformation*. When the substrate responds in a purely elastic manner, the impact time, t_0, is [25]:

$$\frac{t_0 v_0}{D} = 2.54\left(\frac{\rho_\mathrm{p} v_0^2}{E_{\mathrm{TBC}}}\right)^{2/5} \tag{5}$$

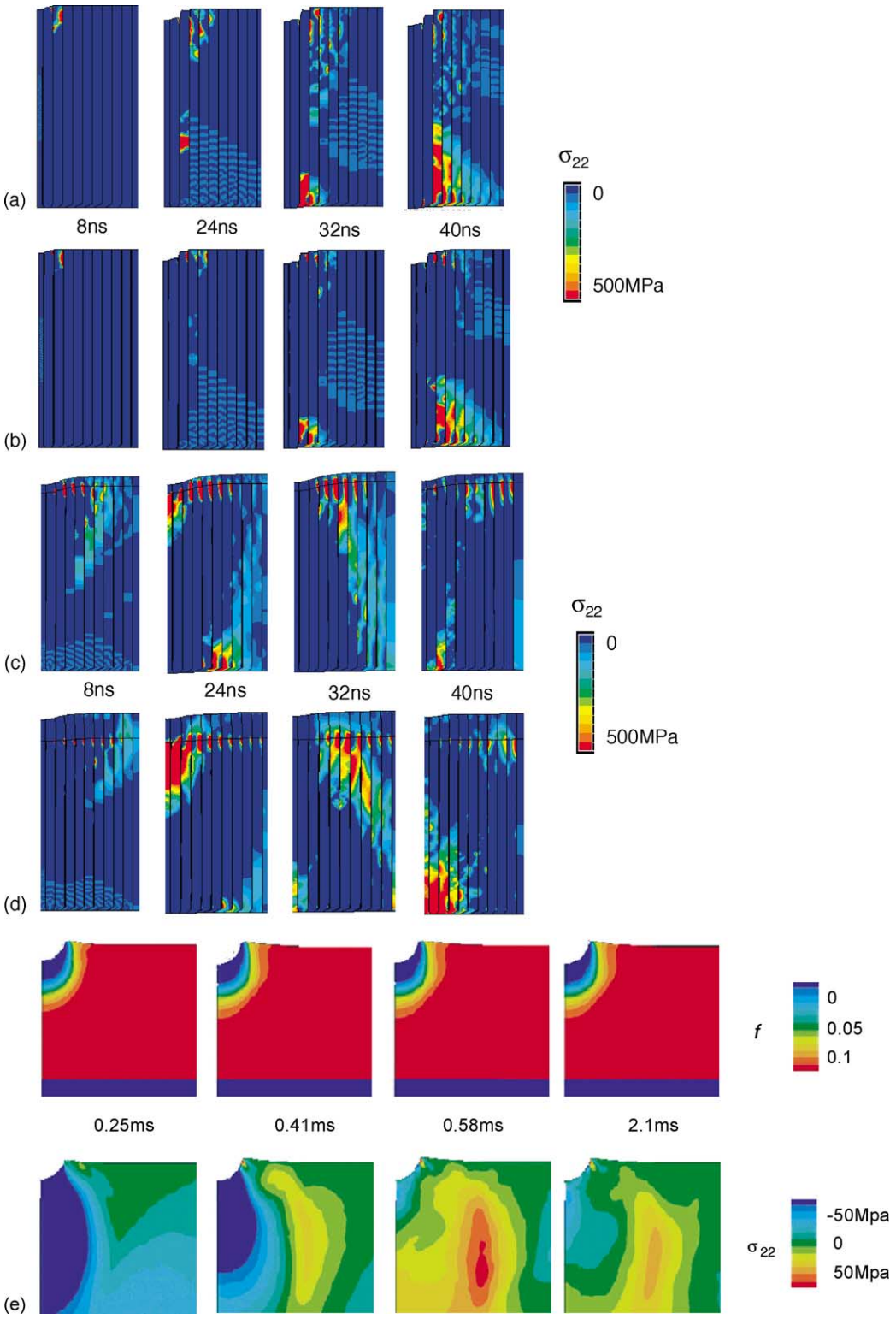
(a)
8ns
24ns
32ns
40ns
σ22
0
500MPa
(b)
(c)
8ns
24ns
32ns
40ns
σ22
0
500MPa
(d)
0.25ms
0.41ms
0.58ms
2.1ms
f
0
0.05
0.1
(e)
σ22
-50Mpa
0
50Mpa

The maximum penetration of the projectile is

$$\frac{\delta_{\max}}{D} = 0.86\left(\frac{\rho_p v_0^2}{E_{TBC}}\right)^{2/5} \quad (6)$$

The stresses that develop have the functional form:

$$\frac{\sigma_{ij}(t,r,z)}{(\rho_p v_0^2)^{1/5} E_{TBC}^{4/5}} = f_{ij}\left(\frac{tv_0}{D}, \frac{r}{D}, \frac{z}{D}\right) \quad (7)$$

where the function f_{ij} is to be ascertained by numerical procedures.

6. Synopsis of dynamic response

Preliminary simulations highlight the following temporal sequence (Fig. 5). Upon initial impact, prior to formation of a plastic wave, an elastic compression wave propagates down the columns beneath the impacting projectile and reaches the interface with the TGO in about 30 ns (Fig. 5a). Thereafter, diffuse reflections occur from the interface, manifest as tensile waves that propagate back toward the free surface. Simultaneously, commencing after ~5–10 ns, the tops of the columns adjacent to the projectile experience bending (Fig. 5a and b). The associated stresses persist for relatively long periods (up to ~100 ns). These bending deformations accommodate the projectile as it penetrates the surface, with amplitude and extent dictated by the presence or absence of a dense layer. The bending effects occur with and without inter-columnar friction. They occur at sufficiently small times that the stresses ascertained using rate-dependent plasticity (Fig. 4) are the same as those determined using only elasticity. For typical impact conditions, the stresses can be large (several GPa), but transient and locally confined near the surface. They are only capable of removing small amounts of material.

At longer times (after about 50 ns), when the impact velocity and temperature are sufficiently large, a well-defined plastic wave propagates from the contact site, followed by a densification wave (Fig. 5c). These zones continue to develop for about 1 ms, until the particle rebounds. Their extent is dictated by the TBC yield strength, $\sigma_Y^{TBC}(0)$. The plastic zone induces residual stresses that scale with $\sigma_Y^{TBC}(0)$, having peak values much smaller than the stresses caused by elastic bending of the columns earlier in the impact sequence. However, when the plastic zone penetrates deeply into the TBC, the large spatial extent of the stresses are more damaging, by virtue of their ability to form kink bands and large-scale delamination (Fig. 2c). The relative importance of short duration column bending and longer duration plastic penetration depend on the kinetic energy of the projectile, the temperature and the composition of the TBC.

In the following sections, stresses and energy release rates are determined for distinct scenarios. The column bending near the surface is analyzed as a dynamic elastic phenomenon responsible for inter-columnar cracks and small-scale material removal. The scenario embraces Domains II and III. The large-scale stresses caused by deep zones of plastic deformation and densification are assessed as a basis for understanding delamination cracks and FOD (Domain I). These results are used in a separate article to formulate a mechanism map [15].

7. Stresses

7.1. Dynamic column bending

Calculations of column bending effects emphasize the σ_{22} stresses causing the inter-columnar cracks that remove material. In the presence of a dense layer, Domain II, the stresses have the spatial and temporal characteristics depicted in Figs. 5 and 6. In each column, tension occurs on that side remote from the impact site, compression on the side closest to the impact, with linear variation across the width. The stresses vary spatially, reaching their highest value on the third column and then diminishing with distance from the impact site. The largest normal stress on this (third) column

Fig. 5. Time sequences for representative impacts showing the evolution of the σ_{22} tensile stresses in the columns. (a) Elastic impact in Domain III, with a frictionless inter-columnar interface. The bending/tension wave that propagates in column (3) acts as a traveling fiducial demarking the propagation of the stress wave from the impact. Note that the stress wave reaches the TGO after 32 ns, whereupon a diffuse tensile wave forms upon reflection of the compressive waves in each of the other columns affected by the impact. The bending effects at the tops of the columns closest to the impact site are evident. They initiate at ~5 ns and persist until 80 ns (particle diameter, $D = 20\,\mu m$; density, $\rho_p = 4000\,kg/m^3$; impact velocity, $v_0 = 300\,m/s$). (b) Elastic impact in Domain III, with an inter-columnar interface subject to a friction coefficient of unity. Again, the stress wave reaches the TGO within 32 ns and reflects as a diffuse tensile wave. The bending at the tops of the columns closest to the impact site now occurs in the opposite direction to (a). But the magnitudes and durations are similar (particle diameter, $D = 20\,\mu m$; density, $\rho_p = 4000\,kg/m^3$; impact velocity, $v_0 = 300\,m/s$). (c) The elastic/plastic impact of a TBC with a 5 μm densified layer representing Domain II. The yield strength has the strain-rate characteristics shown in Fig. 4, with strength at low strain rate, $\sigma_Y^{TBC}(0) = 100\,MPa$. Note the large bending stresses induced at the intersection between the dense and columnar layers occurring at short times (5–50 ns), prior to the development of a plastic wave (particle diameter, $D = 50\,\mu m$; density, $\rho_p = 4000\,kg/m^3$; impact velocity, $v_0 = 300\,m/s$). (d) The elastic/plastic impact of a TBC with a 15 μm densified layer. Again, strain-rate-dependent yielding is used with $\sigma_Y^{TBC}(0) = 100\,MPa$. The bending stresses induced at the intersection between the dense and columnar layers are smaller than in (c) by about a factor 3 (particle diameter, $D = 50\,\mu m$; density, $\rho_p = 4000\,kg/m^3$; impact velocity, $v_0 = 300\,m/s$). (e) An impact in Domain I showing the evolution of the densified zone, the plastic zone and the σ_{22} stresses. Note that rebound occurs after about 1 ms. The largest stresses occur at the interface with the TGO after about 0.58 ms, but they are only slightly in excess of the residual stresses (particle diameter, $D = 100\,\mu m$; density, $\rho_p = 4000\,kg/m^3$; impact velocity, $v_0 = 150\,m/s$).

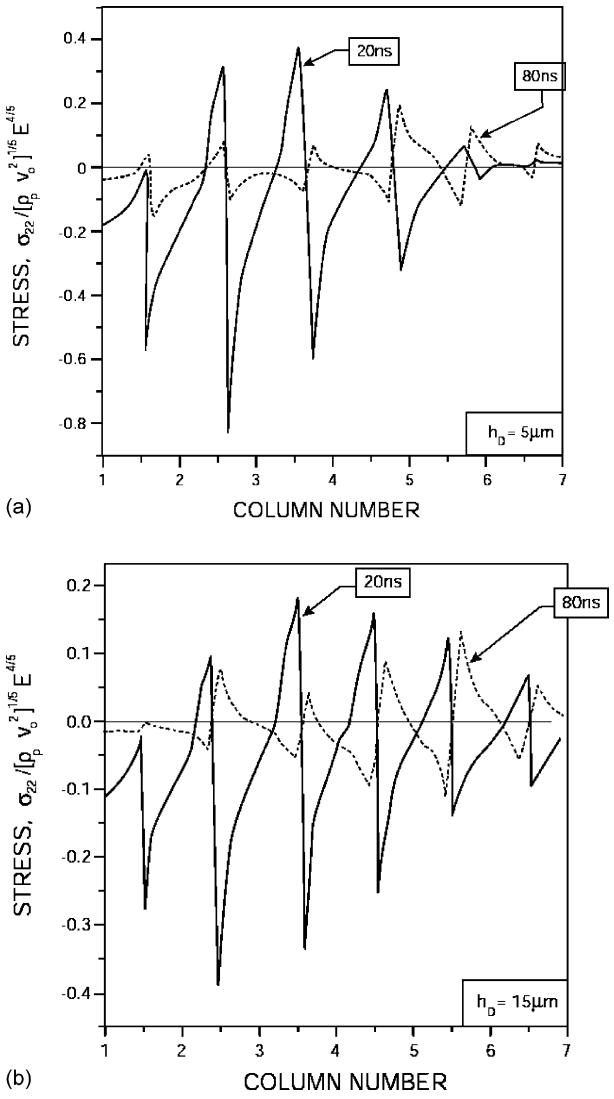

Fig. 6. Temporal variations in the σ_{22} stresses in the columns at short times, prior to plastic wave formation. The responses are exemplified by results obtained within Domain II, in the presence of a thin densified layer. The stresses shown are the tensions at the intersection between the dense and columnar layers after 20 and 80 ns. Results are presented for two different thickness of the dense layer: (a) $h_D = 5\,\mu m$, (b) $h_D = 15\,\mu m$. Note that the stresses are smaller for the thicker layer.

for a 5 μm thick dense layer reaches, $\sigma_{22}/E_{TBC} = 6.0\times10^{-2}$ (or $\sigma_{22} = 8$ GPa). For 15 μm thick dense layer, the highest tensile stress is much smaller, $\sigma_{22}/E_{YSZ} = 2.1\times10^{-2}$. The scaling of the stress with dense layer thickness thus has the approximate form: $\sigma_{22} \sim 1/h_D$. In all columns, the stress decays systematically with time, reaching quite low levels after 80–100 ns. Note that, for the thicker dense layer, the bending changes sign after 80 ns (tension on the side closest to the impact). Calculations performed at different gap width (in the range 0.1–0.3 μm) and for larger column width ($d = 10\,\mu m$) revealed minimal influence.

Additional insight can be obtained by plotting the stress range acting on each column (Fig. 7), $\Delta\Sigma \equiv \Delta\sigma_{22}/(\rho_p v_0^2)^{1/5} E_{TBC}^{4/5}$ (maximum tension to maximum compression) and the mean stress averaged across the column (Fig. 8), $\bar{\Sigma} \equiv \bar{\sigma}_{22}/(\rho_p v_0^2)^{1/5} E_{TBC}^{4/5}$. That the largest tensile stress due to bending occurs on the third column (at ~20 ns) is vividly apparent from Figs. 6–8. Note that, at longer times, the largest stress shifts to columns further from the impact, especially when the dense layer is thicker ($h = 15\,\mu m$). This variation in stress amplitude is an essential input to the material removal criterion, discussed in the next section. The changes in the average stress with location and time are revealing (Fig. 8). This average appears to oscillate from primarily compressive to tensile at intervals of

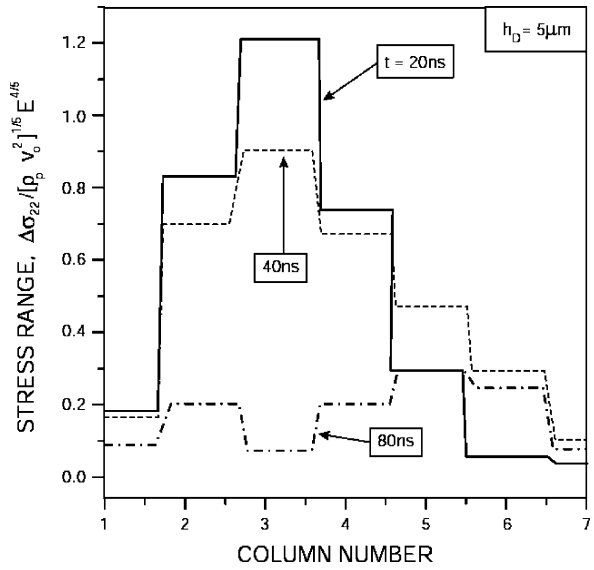

Fig. 7. The results from Fig. 6 re-expressed as the normalized bending stress amplitude $\Delta\sigma_{22}$ on the first seven columns at several intervals after impact.

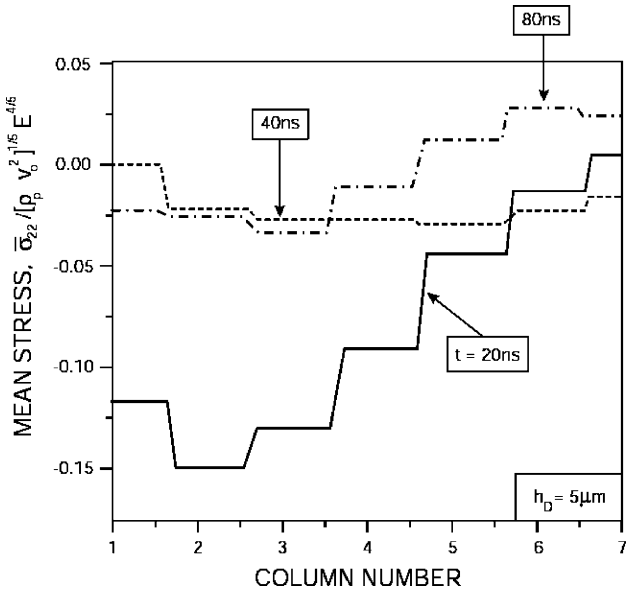

Fig. 8. The results from Fig. 6 re-expressed as the average stress, $\bar{\sigma}_{22}$, on the same columns at several times after impact.

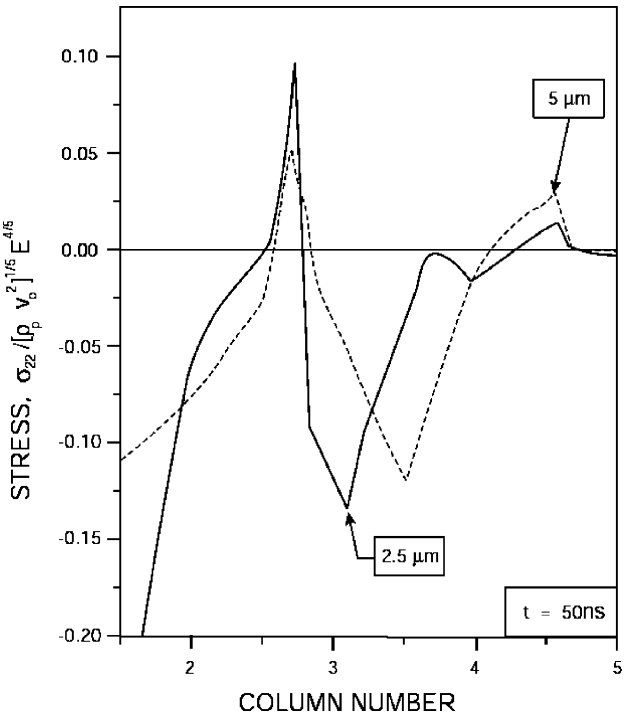

Fig. 9. Transient σ_{22} stresses in the columns at 50 ns, prior to plastic wave formation in Domain III. The tensile stresses are shown at 2.5, 5, and 15 μm below the free surface.

about 20 ns, starting in compression at 20 ns. This change in mean stress biases the incidence of column cracking.

The corresponding bending effects in the absence of a dense layer are apparent in Figs. 5 and 9. The most substantive transient tensile σ_{22} stresses are those confined on the top of TBC columns, adjacent to the impact site, caused by the localized bending of the columns as the particle penetrates (Fig. 1c). When the inter-columnar interface is frictionless, and when the impacting particle has diameter, $D = 20\,\mu\text{m}$ ($D = 4d$), the largest bending stresses occur in the 4th and 5th columns (Figs. 5a and 9), on the side closest to the impact. At 5 μm below the surface, the largest normal stress on the fifth column (Fig. 9) reaches, $\sigma_{22}/E_{\text{TBC}} = 3.0 \times 10^{-2}$ (or $\sigma_{22} = 4\,\text{GPa}$). At 15 μm below, the highest tensile stress occurs on the 4th column, $\sigma_{22}/E_{\text{TBC}} = 4.0 \times 10^{-2}$ (or $\sigma_{22} = 5.6\,\text{GPa}$). These stresses can be large enough to fracture the tops of the columns, as discussed below. When a high level of Coulomb friction is imposed at the inter-columnar interfaces ($\mu = 1$) bending still occurs (Fig. 5a), with associated susceptibility to cracking. However, for the equivalent impact, the predominant tensile stress occurs on the *opposite side* of the columns (Fig. 5b). Moreover, the stresses are lower when friction operates. Exploring the salient details will be the subject of continuing analysis.

A comparison indicates that the presence of the dense layer elevates the largest tensile stresses, while also inducing tension over a larger number of columns. The thicker the dense layer, the lower the stresses. Accordingly, column cracking in Domain II will be influenced by the TBC yield strength, given its effect on the layer thickness, which from (3) and (4), is

$$h_{\text{D}} \approx 2.4D\sqrt{\sqrt{\Omega}(0.1 + 0.84\sqrt{\Omega})} \tag{8}$$

Recall that $\Omega = (\pi/12)[\rho_{\text{p}}/\sigma_Y^{\text{TBC}}(0)]v_0^2$.

7.2. Plastic penetration and residual stresses

In Domain I, the delaminations are largely governed by the residual stresses [11]. Such stresses have been analyzed previously and comprehensively discussed for quasi-static indentation [16–18]. Two basic results from prior studies are summarized:

(i) When the impact conditions are such that the plastic zone is confined within the TBC, a threshold condition must be exceeded before cracks can form, expressed by an index [16]:

$$\Delta_{\text{th}} = \frac{\sigma_y^{\text{th}}(\delta_{\max}D)^{1/4}}{\sqrt{E_{\text{TBC}}\Gamma_{\text{TBC}}}} \tag{9}$$

Large-scale cracks form when $\Delta_{\text{th}} \geq 0.3\times10^{-2}$ [16,17]. Based on the yield strength of the TBC at 1150 °C (Fig. 3) and estimates of its mode I toughness [20] (9) predicts that penetrations as deep as $\delta_{\max} \approx 25\,\mu\text{m}$ should be possible before cracks form in the TBC. This threshold condition is consistent with the observations that, when shallow (≤20 μm), plastic zones are not accompanied by large-scale cracks (Fig. 2a and d). Instead they create a dense zone that then becomes susceptible to removal by subsequent impacts.

(ii) When the plastic zone extends through the TBC to the interface with the TGO, delamination cracks tend to nucleate at kink bands and extend just above the TGO. Once nucleated, the extension of these cracks along the interface exhibits the following dependence on material properties [11]:

$$\frac{a_{\text{delam}}}{H_{\text{TBC}}} \sim \left[\frac{(\sigma_Y^{\text{TBC}})^2 H_{\text{TBC}}}{E_{\text{TBC}}\Gamma_{\text{TBC}}}\right]\left[\frac{\sigma_Y^{\text{TBC}}}{E_{\text{TBC}}}\right]^{\alpha}\left\{\frac{\rho_{\text{p}}v_0^2}{\sigma_Y^{\text{TBC}}}\right\}^{\beta} \tag{10}$$

where $\alpha \approx 1$, $\beta \approx 1/4$. This result suggests a delamination index, $\Xi_1 = \Gamma_{\text{TBC}}E_{\text{TBC}}^2/(\sigma_Y^{\text{TBC}})^3$: that is, once delaminations have been nucleated, the material removal rate decreases with lower yield strength and higher toughness. Since this result only appears to apply whenever the TBC is thin enough for the plastic zone to penetrate, delamination may only arise after the TBC has been partially thinned by prior erosion (Fig. 2c).

New calculations explore dynamic effects that cause cracks parallel to the impact surface to form within the densified zone (Fig. 2d). For such cracks to form, stress component in the direction normal to the impact surface must develop at some stage during the impact event. Such tensions do not exist under normal impact conditions. They

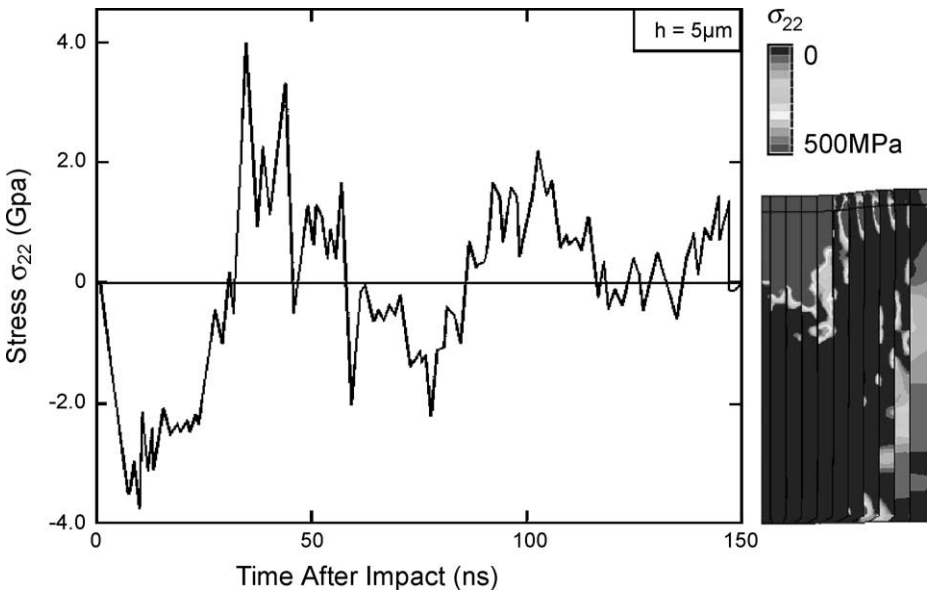

Fig. 10. Time sequence for the stress normal to the impact plane σ_{22} near the surface caused by an impacting particle that adheres to the TBC. The insert shows the contours of tensile stress.

are believed to arise when the particle adheres to the surface during penetration. Then, upon rebound, the reflected stress waves create tension in the dense zone. The results of calculations that allow the particle to adhere to the TBC at the instant of maximum penetration (Fig. 10) affirm the presence of large tensile stresses. The implication is that particle/TBC adhesion during impact is another factor affecting erosion. This is another topic for future investigation.

8. Column cracking and erosion

Since the column bending duration is well in excess of the minimum needed to activate small cracks [26], the column cracking phenomenon can be envisaged as quasi-static. The cracks are considered to emanate from flaws, length a_0 at the column edges (especially the "feathery" porosity, Fig. 11) [27]. The tendency for such cracks to extend across the columns and detach material differs in Domains II and III. Absent a dense layer, the tops of the bending columns can displace, allowing the cracks to open and extend across the column, removing material. When a dense layer is present, its stiffness inhibits opening, stabilizing the cracks, enabling them to arrest without fully separating the columns. Consequently, while the stresses induced in Domain II may exceed those in Domain III, material removal rates may be lower. Comprehensive models of these mechanisms are beyond the scope of the present study. Instead, scaling results are derived that identify the salient material property combinations.

In *Domain III*, stress intensity factors can be ascertained from standard results for beams in bending. Since the stresses acting across the prospective crack trajectory are a combination of bending, $\Delta\Sigma$, with superposed tension or compression, $\bar{\Sigma}$, the loading is represented by a bending moment and axial force. The mode I stress intensity factor is given by [28]:

$$K_{\mathrm{I}} \approx \sqrt{\pi a_0}[\Delta\sigma_{22} + \bar{\sigma}_{22}], \qquad G \approx \frac{\pi a_0}{E_{\mathrm{TBC}}}[\Delta\sigma_{22} + \bar{\sigma}_{22}]^2 \tag{11}$$

A criterion for column detachment can be derived upon equating the energy release rate to the inter-columnar

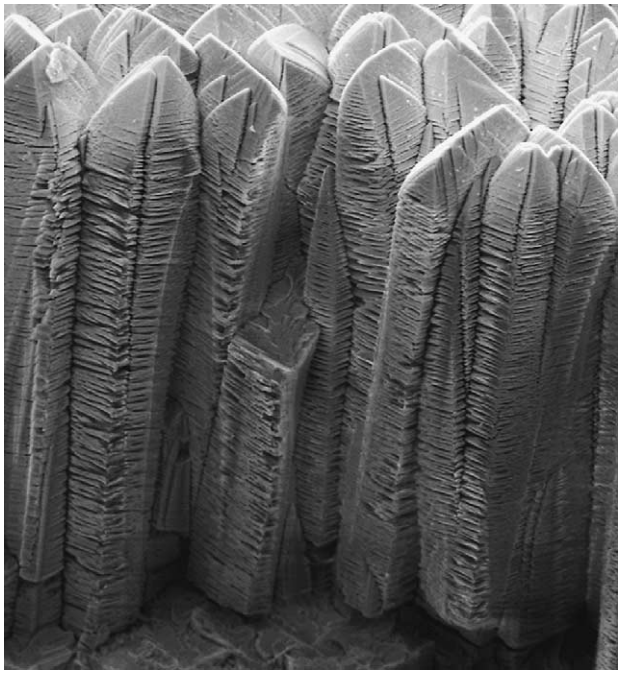

Fig. 11. The "feathery" porosity in the columns regarded as the flaws that initiate inter-columnar cracking [27].

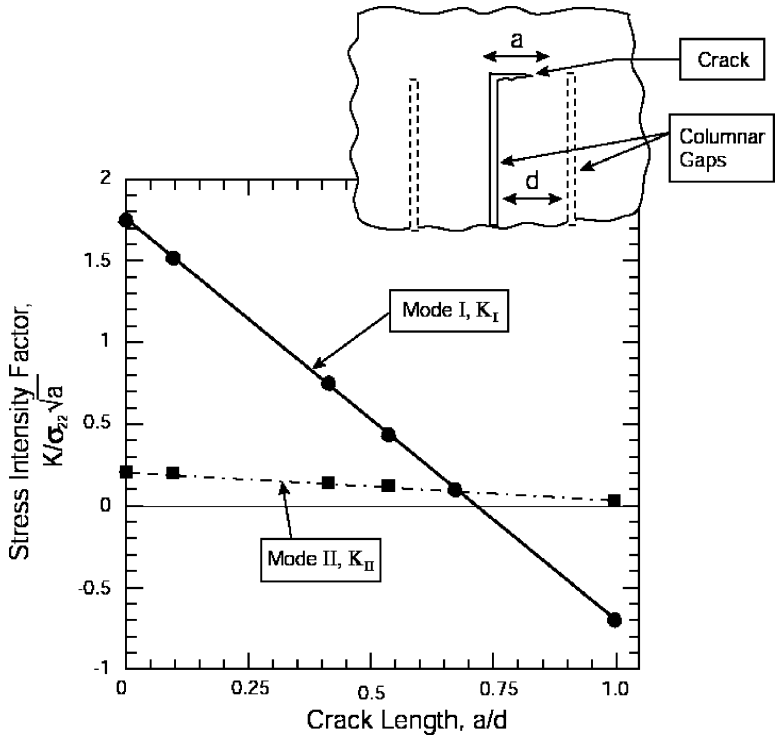

Fig. 12. The stress intensity factors (modes I and II) for a kink crack extending beneath the dense layer between two adjacent columns.

toughness, Γ_{TBC} [28]. By using (7) to scale the stresses, and when a_0 scales with the column diameter, d, the criterion becomes:

$$\pi[\bar{\Sigma} + \Delta\Sigma]^2 \geq \frac{\Gamma_{\mathrm{TBC}}}{(\rho_{\mathrm{p}} v_0^2)^{2/5} E_{\mathrm{TBC}}^{3/5} d} \tag{12}$$

This inequality defines an erosion index, $\Xi_3 \equiv \Gamma_{\mathrm{TBC}}/E_{\mathrm{TBC}}^{3/5} d$, having the feature that the larger Ξ_3, the lower the erosion rate.

In *Domain II*, the gap between the columns responds as a vertical crack with a kink that extends along the dense/columnar intersection, parallel to the surface. The stress intensity factors at zero mean stress, determined using finite elements (Fig. 12), can be expressed in the form:

$$\frac{K_{\mathrm{I}}}{\Delta\sigma_{22}\sqrt{a}} = 1.76 - \frac{2.42a}{b} \quad \frac{K_{\mathrm{II}}}{\Delta\sigma_{22}\sqrt{a}} = 0.20 - \frac{0.17a}{d} \tag{13}$$

In pure bending, $K_1 \to 0$ at $a/d = 0.75$, indicating that the crack must close at that length. The outcome would be a crack that arrests without detaching the dense layer from the column. To crack across the column, a mean tensile stress must be present, as evident in some of the columns (Fig. 7). The mode I stress intensity due to a superposed mean tensile stress is: $K_{\mathrm{I}}/\bar{\sigma}_{22}\sqrt{a} = 1.76$. Complete separation of the dense layer only occurs when the net mode I stress intensity factor as $a/d \to 1$ exceeds the fracture toughness of the TBC columns. Using (7) to establish the stress scaling and recalling that the stresses vary as, $\sigma_{22} \sim 1/h_{\mathrm{D}}$, the erosion index becomes, $\Xi_2 \equiv \Gamma_{\mathrm{TBC}}/E_{\mathrm{TBC}}^{3/5} d\sigma_Y^{\mathrm{TBC}}$. That is, the larger the magnitude of this index, the lower the erosion rate. Note that, unlike Domain III, the yield strength of the TBC affects the erosion rate, because of its role in affecting the thickness of the densified zone.

9. Concluding remarks

The impact of thermal barrier coatings by hard projectiles at high temperature has been analyzed. Three different domains have been explored governed by particle size, velocity, temperature and TBC composition.

Domain I represents impact conditions wherein the projectile creates deeply penetrating plastic/densification zones. This domain pertains when the impacting particles are large and have high velocity, provided that the temperature is large enough for the TBC to be relatively soft. In this case, short time elastic effects are relatively unimportant and the response is dominated by conditions that obtain after about 1 ms, at particle rebound. When the plastic zone is confined within the oxide, a threshold condition must be exceeded before large-scale cracks can be induced by the residual stress field. At 1150 °C, typical impacts do not exceed the threshold, whereupon a dense layer is created without forming delaminations. However, for TBCs partially thinned by erosion, similar impacts produce kink bands that nucleate delaminations (Fig. 2c). In such cases, interactions with the bond coat might be important, but

remain to be analyzed. In such circumstances, the index governing the extent of material removal by delamination is [11]: $\Xi_1 \equiv \Gamma_{\mathrm{TBC}} E_{\mathrm{TBC}}^2/(\sigma_Y^{\mathrm{TBC}})^3$. Large values of this index correspond to small material removal rates.

Domain II refers to impact conditions that produce relatively shallow densified zones, exemplified by the impact of intermediate sized particles into relatively soft TBCs. In this case, the plastic/densification wave effects that culminate at rebound are relatively benign. Now, elastic effects occurring at short times (5–30 ns) are more important. These are manifest in the bending of the tops of the nearby columns to accommodate the penetration of the projectile. The largest stresses occur at the intersection of the dense and columnar layers and can be large enough to form cracks that remove small amounts of material. The susceptibility of the TBC to material removal is governed by the erosion index: $\Xi_2 \equiv \Gamma_{\mathrm{TBC}}/E_{\mathrm{TBC}}^{3/5} d\sigma_Y^{\mathrm{TBC}}$. Large values of this index result in diminished material removal rates.

Domain III arises when the TBC responds in an entirely elastic manner. This condition is operative for small particle impact, especially at lower temperatures. Again, bending effects at the tops of the columns that arise at short times are most important. The erosion index is, $\Xi_3 \equiv \Gamma_{\mathrm{TBC}}/E_{\mathrm{TBC}}^{3/5} d$.

Other material removal modes also exist and remain to be analyzed.

References

[1] R.A. Miller, J. Am. Ceram. Soc. 67 (1984) 517–524.
[2] N. Padture, M. Gell, E. Jordan, Science 296 (2002) 280–284.
[3] M.J. Stiger, N.M. Yanar, M.G. Toppings, F.S. Pettit, G.H. Meier, Z. Metall. 90 (1999) 1069–1082.
[4] J.A. Ruud, A. Bartz, M.P. Borom, C.A. Johnson, J. Am. Ceram. Soc. 84 (2001) 1545–1552.
[5] A.G. Evans, D.R. Mumm, J.W. Hutchinson, G.H. Meier, F.S. Pettit, Prog. Mater. Sci. 46 (2001) 505–553.
[6] D.R. Mumm, A.G. Evans, I.T. Spitsberg, Acta Mater. 49 (2001) 1793–1804.
[7] I.T. Spitsberg, D.R. Mumm, A.G. Evans, J. Mater. Res., in press.
[8] A.M. Karlsson, J.W. Hutchinson, A.G. Evans, J. Mech. Phys. Solids 50 (2002) 1565–1589.
[9] P.K. Wright, A.G. Evans, Curr. Opin. Solid State Mater. Sci. 4 (1999) 255–268.
[10] S.R. Choi, J.W. Hutchinson, A.G. Evans, Mech. Mater. 31 (1999) 431–447.
[11] X. Chen, R. Wang, N. Yao, A.G. Evans, J.W. Hutchinson, R.W. Bruce, Mater. Sci. Eng. A 352 (2003) 221–231.
[12] J.R. Nicholls, M.J. Deakin, D.S. Rickerby, Wear 233–235 (1999) 352–361.
[13] R.G. Wellman, J.R. Nicholls, Wear 242 (2000) 89–96.
[14] R.W. Bruce, Tribol. Trans. 41 (1998) 399–410.
[15] X. Chen, A.G. Evans, J.W. Hutchinson, in press.
[16] B.R. Lawn, Fracture of Brittle Solids, Cambridge University Press, Cambridge, 1993.
[17] B.R. Lawn, A.G. Evans, J. Mater. Sci. 12 (1977) 2195–2201.
[18] B.R. Lawn, D.B. Marshall, A.G. Evans, J. Am. Ceram. Soc. 63 (1980) 574–580.
[19] D.R. Mumm, M. Watanabe, A.G. Evans, J.A. Pfaendtner, Acta Mater., in press.
[20] M. Watanabe, A.G. Evans, Unpublished.
[21] B.D. Kernan, A. He, A.H. Heuer, J. Am. Ceram. Soc., in press.
[22] M.W. Chen, R.T. Ott, T.C. Hufnagel, P.K. Wright, K.J. Hemker, Surf. Coat. Technol. 163–164 (2003) 25–30.
[23] ABAQUS Version 5.8 User's Manual, Hibbit, Karlsson and Sorensen Inc., Pawtucket, RI, 1998.
[24] X. Chen, J.W. Hutchinson, J. Mech. Phys. Solids 50 (2002) 2669–2690.
[25] K.L. Johnson, Contact Mechanics, Cambridge University Press, Cambridge, 1985.
[26] L.B. Freund, Dynamic Fracture Mechanics, Cambridge University Press, Cambridge, 1990.
[27] S.G. Terry, C. Levi, Mater. Sci. Eng., in press.
[28] H. Tada, P.C. Paris, G.R. Irwin, The Stress Analysis of Cracks Handbook, ASME Press, New York, 2000.